Science Advances
AAAS

Supplementary Materials for

No ordinary proteins: Adsorption and molecular orientation of monoclonal antibodies

Ankit Kanthe, Andrew Ilott, Mary Krause, Songyan Zheng, Jinjiang Li, Wei Bu, Mrinal K. Bera, Binhua Lin, Charles Maldarelli*, Raymond S. Tu*

*Corresponding author. Email: cmaldarelli@ccny.cuny.edu (C.M.); tu@ccny.cuny.edu (R.S.T.)

Published 27 August 2021, *Sci. Adv.* **7**, eabg2873 (2021)
DOI: 10.1126/sciadv.abg2873

This PDF file includes:

Supporting Information Text

Pendant bubble area change past the induction period

As noted from Fig. 2a of the main text, an induction period is observed for low bulk mAb concentrations, 7.0 $\times$ 10^{-5} - 1.0 $\times 10^{-3}$ mg/mℓ, where the tension remains nearly constant at the 'clean' (i.e., buffer only) interface value before relaxing sharply. As molecules adsorb to the surface past the induction time lowering the tension, the surface area of the pendant bubble may increase due to adsorption thereby elongating the shape of the pendant bubble. To indicate these pendant bubble surface area changes before and after the induction period, pendant bubble images for mAb concentration of 5.0 $\times$ 10^{-4} mg/mℓ are used to generate Fig. S1.

Figure S1 shows that during the induction period, which lasts for around 2000 s (blue dashed line) for 5.0 $\times$ 10^{-4} mg/mℓ mAb bulk concentration, the bubble area (orange line) did not record a significant change thereby maintaining the tension value at buffer only interface value of 72.5 mN/m. As time progresses, the tension continues to decrease due to adsorption of protein molecules that causes a change in the bubble area (increased from 33.42 mm^2 to 33.66 mm^2, i.e., 0.72 % increase in area, Figure S1a). The calculated changes in the surface tension on protein adsorption are calculated using these dynamic values for the area. As adsorption continues, the bubble area increases, lowering the tension value.

X-ray reflectivity data analysis

The reflectivity profile represented in Fig. 3a of the main text is normalized using the Fresnel Reflectivity $R_F(Q_z)$ of water. $R_F(Q_z)$ refers to the reflectivity profile from an ideally smooth surface with a step-function based electron density profile (EDP). The normalization of the obtained reflectivity profile helps to calculate the thickness of the adsorbed layer and the structural features of the molecules in the form of oscillations at the interface. The electron density profile that gives an estimate of the thickness and the adsorbed amount at the interface is obtained using the normalized reflectivity profile using the slab-model based on Parratt formalism. More details on this are provided elsewhere $(44, 45)$.

Briefly, the normalized reflectivity data is fitted by assuming a constant electron density with a thickness value appropriate for the system. The initial guess for the thickness is chosen to be greater than the length of the mAb (200 Å). This thickness layer is further sub-divided into additional sub-layers, each layer associated with an electron density, thickness and roughness. This initial EDP then undergoes an iterative procedure to minimize the mean square variation (χ^2). χ^2 represents the difference between the calculated and the experimental XR curves. In order to test the convergence of this fitting procedure and obtain a unique EDP, the above process is repeated using different initial guesses for electrons density. The EDP from this model-independent approach is then used as an intial guess for the slab-model to get a smooth EDP.

Calculation of the Surface Concentration for mAb system

The surface concentration at each mAb bulk concentration (7.0 $\times$ 10^{-5} mg/mℓ - 1.0 mg/mℓ) is calculated based on the total volume balance at the interface and the total electron density balance, where, the subscript, p and w, denote protein (mAb) and water, $\mathcal{V}$ is the molecular volume, Γ is the surface concentration, e is the number of electrons, MW is the molecular

weight and $\mathcal{N}_\mathcal{A}$ is the Avogadro's number. The interfacial depth d and the total number of electrons per unit area, e_T are obtained from the EDP profile (Fig. 3b of the main text). d is taken as the depth where the electron density profile reaches the electron density of water, and e_T is the integrated area under the EDP curve. The parameters such molecular weight, molecular volume and number of electrons for protein and water are given in the Supporting Information, Table S1. The above two equations are solved simultaneously to calculate Γ_p and Γ_w.

$$d = \frac{\mathcal{N}_\mathcal{A}}{MW_p}\Gamma_p\mathcal{V}_p + \frac{\mathcal{N}_\mathcal{A}}{MW_w}\Gamma_p\mathcal{V}_w$$
$$e_T = \frac{\mathcal{N}_\mathcal{A}}{MW_p}\Gamma_p e_p + \frac{\mathcal{N}_\mathcal{A}}{MW_w}\Gamma_w e_w$$

Homology modeling and estimate of antibody size

The 3D atomic structure of mAb was generated from the antibody sequence using the standard homology modeling protocol (55) in the MOE software (53). Template protein structures with high sequence similarity to each domain and the complementarity-determining region (CDR) loop in the mAb are sought and scored based on the similarity and the quality of the template structure. The model is built from a combination of the highest scoring templates, with the CDR loop templates grafted onto the V_L and V_H frameworks. A molecular mechanics energy minimization using the Amber10 force field $(56, 57)$ is then performed on the model to further refine the atomic coordinates and relieve strained geometries. The dimensions of the Fab and Fc domains, as well as the overall extent of the antibody are shown in Fig. S1. They were estimated by measuring the relevant inter-atomic distances from the homology model.

Two-population fit for simulated EDP

To explain the possibility of two populations for mAb adsorption in the condensation region, homology modeling is used. A theoretical EDP is computed assuming a population of a flat-on configuration (θ = 80 and ϕ = 180) with population fraction X, and a population with orientation θ and ϕ and fraction (1-X). For each angle pair and X value, the EDP is computed and compared to the experimental EDP to obtain a RSS. In computing the EDP for the mixed population, the EDP of each population is first computed, and then the two EDPs are summed, weighted by the fractions of each population. This least squared difference is then minimized by varying the percentage of the flat-on configuration, X, and the vertical orientation of both populations to obtain a minimum RSS. The map of this minimum as a function of the assumed θ,ϕ orientation of the second population is given in Fig. 7a of the main text for the two bulk concentrations, and the percentage of flat-on at the minimum for the θ,ϕ of the second population is given in Fig. 7b of the main text.

In Fig. 5b of the main text and Fig. S2 are also given the one- and two- population RSS maps in θ, ϕ space for the higher concentration end of the condensation region, 2.0×10^{-2} mg/mℓ, but at two early times (1 hr, 60 mN/m and 2 hr, 57 mN/m) prior to the quasi-equilibrium at 3 hrs. from Fig. 5b, the one population RSS maps demonstrate again the intermediate behavior in orientation as was the case for the two quasi-equilibrium values for 5.0×10^{-4} mg/mℓ, 61 mN/m

and 2.0×10^{-2} mg/mℓ, 56.8 mN/m, as the tensions and surface concentrations are intermediate between the tensions/concentrations for the quasi-equilibria. The two-population fits in Fig. S3 for these two surface ages show that the average percentage of the flat-on configuration has decreased from 72% (1 hr) to 60% (2 hr) with the quasi-equilibrium percentage at 3 hrs equal to 48%. As these two data sets have tensions and surface concentrations that lie in the range of those in the condensation region, they support the hypothesis that the adsorbed layer consists of two populations, flat-on and either side-on or end-on.

A better visualization of the heat map indicating % of the flat-on contribution from the two-population fit is shown in Fig. S4. At lower bulk mAb concentration (7.0×10^{-5} mg/mℓ (72.5, 70, 67 mN/m)), mAbs are predominantly adsorbed in flat-on orientation (100%). As concentration increases (or surface tension decreases), the contribution from flat-on orientation decreases from 80% (5.0×10^{-4} mg/mℓ (61 mN/m)) to around 48% (2.0×10^{-2} mg/mℓ (56.8 mN/m)), indicating that mAbs are now present in two-population states, one flat-on and one either side-on or end-on orientations. This represents the condensation or rearrangement layer in the surface tension isotherm (Fig. 2b and 4c) defining the two populations for the adsorbed mAb layer. Furthermore, the contribution of flat-on decreases as surface tension decreases (20%) at higher bulk mAb concentrations (5.0×10^{-2} mg/mℓ (55 mN/m), 5.0×10^{-1} mg/mℓ (54 mN/m) and 1.0 mg/mℓ (54 mN/m)) corresponding to the quasi-equilibria surface tension. Therefore, beyond the condensation region, the mAbs are in either tilted side-on or end-on.

Supporting Information Figures

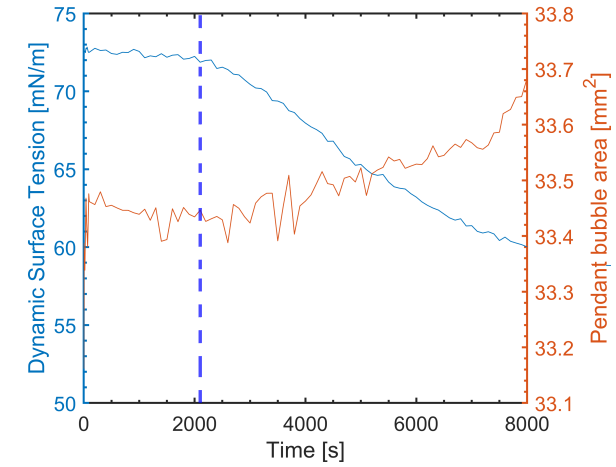

(a)

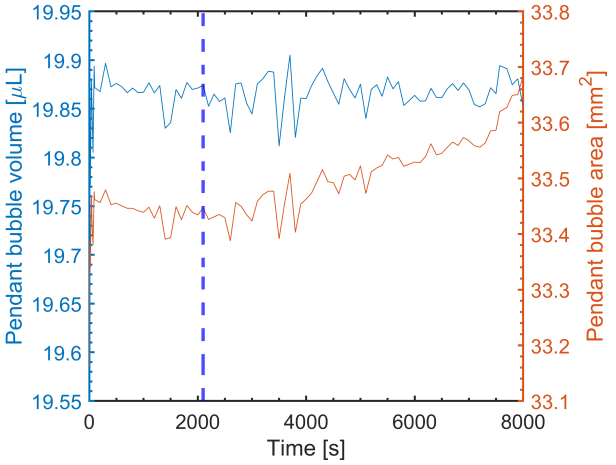

(b)

Figure S1: (a) Dynamic surface tension (blue) and pendant bubble area (orange) change as a function of time for 5.0×10^{-4} mg/mℓ mAb bulk concentration. (b) Pendant bubble volume (blue) and area (orange) change as a function of time. A feedback control loop is used to ensure that the bubble volume remains constant throughout the duration of the experiment. The pendant bubble area change is due to the adsorption of molecules to the surface. The blue dashed line indicates the end of the induction period.

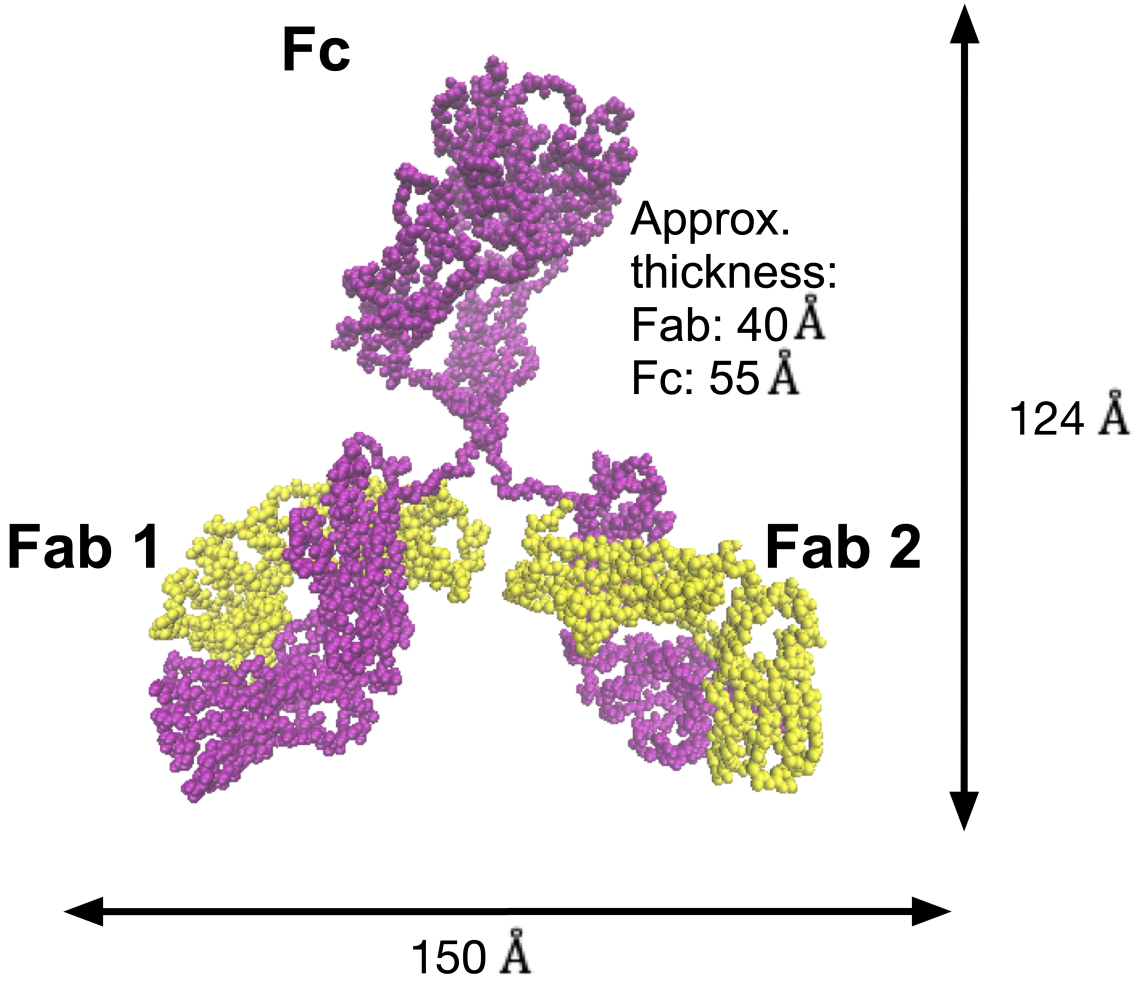

Figure S2: Visualization of the mAb structure and dimensions obtained from the homology model

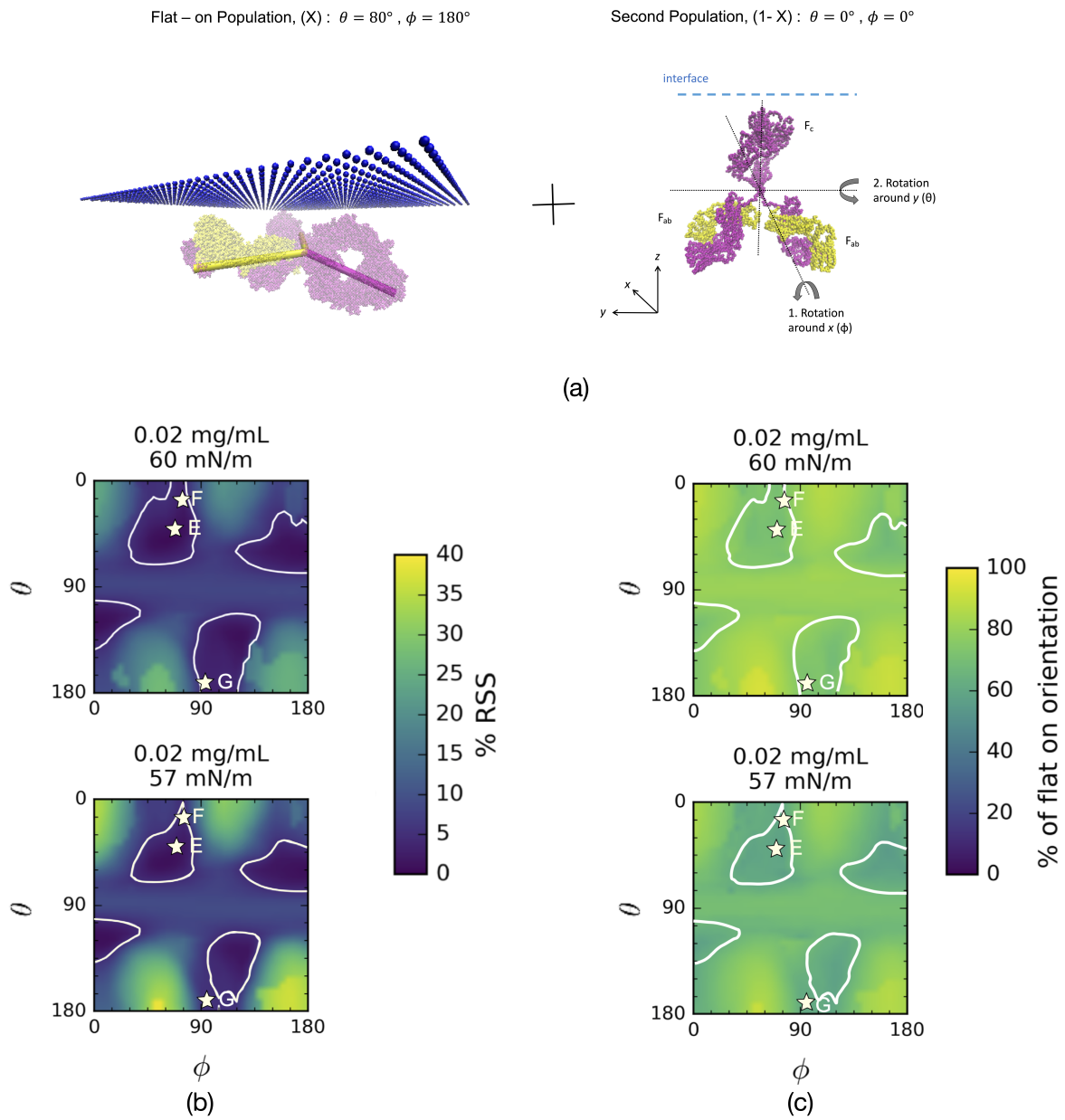

Figure S3: Two-population homology construct to predict the orientation of mAb at the air/water interface in the condensation region. (a) One population with flat-on configuration (θ = 80 and ϕ = 180) and a second with configuration angles θ and ϕ. (b) Minimized residual sum of squares (RSS) map in θ, ϕ space corresponding to the orientation of the second population for 2.0 $\times$ 10^{-2} mg/mℓ: 60 mN/m and 57 mN/m. The RSS has been minimized in the relative fractions of the populations. (c) θ,ϕ maps of the percentage fraction of the flat-on configuration corresponding to the minimized RSS in (b). The asterisks (E, F and G) correspond to the second population indicating tilted side-on orientations of Fig. 5d of the main text.

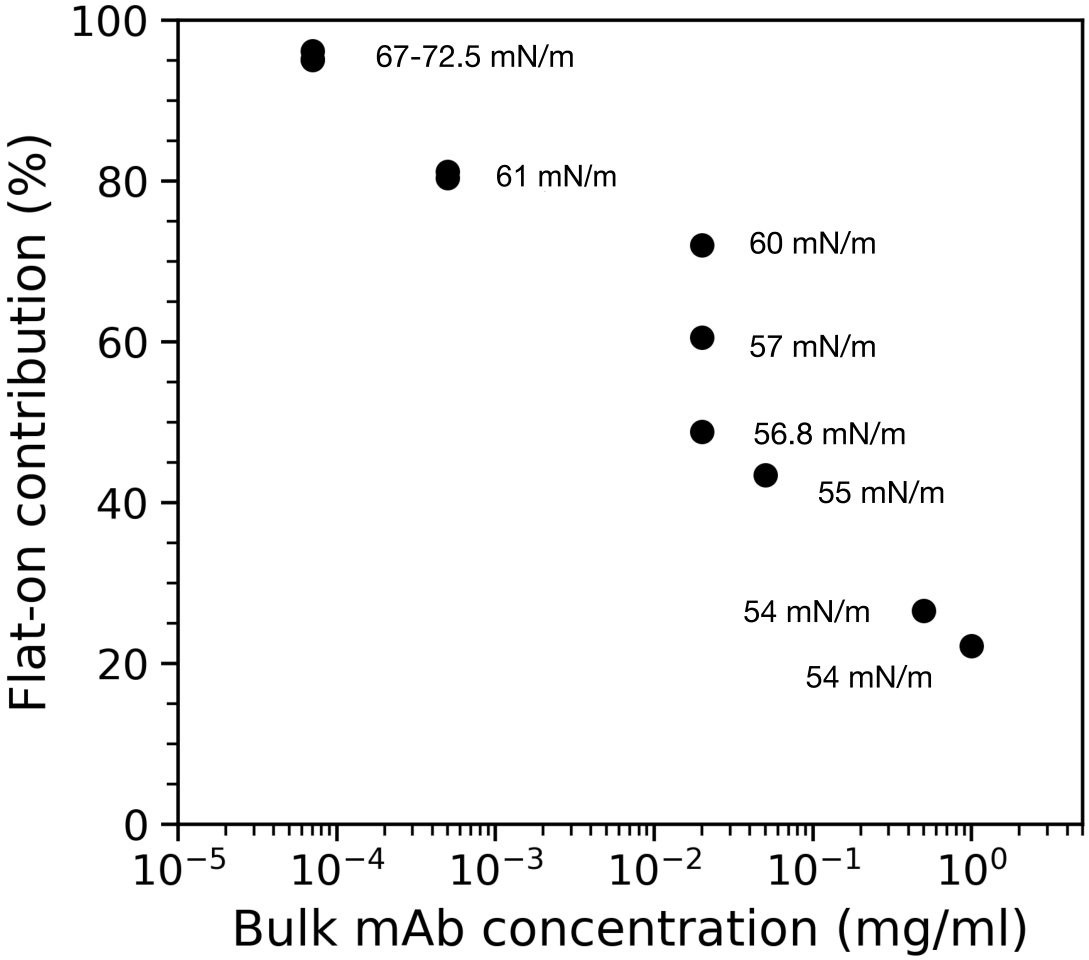

Figure S4: % Flat-on contribution obtained as a function of bulk mAb concentration for the two-population fits. The surface tension corresponding to each mAb concentration is also reported.

Table S1: The molecular weight (MW), number of electrons (e) and molecular volume ($\mathcal{V}$) for the antibody (mAb) and water used in the analysis of XR data.

Component	MW (g/mol)	e	$\mathcal{V}$ (Å^3)
mAb	145526.44	72763	133235.5
water	18	10	30

REFERENCES AND NOTES

1. D. Möbius, R. Miller, *Proteins at Liquid Interfaces* (Elsevier, 1998).

2. Y. F. Yano, Kinetics of protein unfolding at interfaces. *J. Phys. Condens. Matter* **24**, 503101 (2012).

3. M. A. Bos, T. van Vliet, Interfacial rheological properties of adsorbed protein layers and surfactants: A review. *Adv. Colloid Interface Sci.* **91**, 437–471 (2001).

4. E. M. Freer, K. S. Yim, G. G. Fuller, C. J. Radke, Shear and dilatational relaxation mechanisms of globular and flexible proteins at the hexadecane/water interface. *Langmuir* **20**, 10159–10167 (2004).

5. E. Dickinson, R. Miller, *Food Colloids: Fundamentals of Formulation*, vol. 258 (Royal Society of Chemistry, 2001).

6. B. S. Murray, Rheological properties of protein films. *Curr. Opin. Colloid Interface Sci.* **16**, 27–35 (2011).

7. M. Parsa, A. Trybala, D. Malik, V. Starov, Foam in pharmaceutical and medical applications. *Curr. Opin.* **44**, 153–167 (2019).

8. L. Lazzeri, M. G. Cascone, S. Danti, L. P. Serino, S. Moscato, N. Bernardini, Gelatine/PLLA sponge-like scaffolds: Morphological and biological characterization. *J. Mater. Sci. Mater. Med.* **17**, 1211–1217 (2006).

9. J. A. Zasadzinski, P. C. Stenger, I. Shieh, P. Dhar, Overcoming rapid inactivation of lung surfactant: Analogies between competitive adsorption and colloid stability. A Surface View on Membrane Structure, Dynamics and Applications, *Biochim. Biophys. Acta Biomembr.* **1798**, 801–828 (2010).

10. J. M. Reichert, Monoclonal antibodies as innovative therapeutics. *Curr. Pharm. Biotechnol.* **9**, 423–430 (2008).

11. J. Li, M. E. Krause, X. Chen, Y. Cheng, W. Dai, J. J. Hill, M. Huang, S. Jordan, D. LaCasse, L. Narhi, E. Shalaev, I. C. Shieh, J. C. Thomas, R. Tu, S. Zheng, L. Zhu, Interfacial stress in the development of

biologics: Fundamental understanding, current practice, and future perspective. *AAPS J.* **21**, 44 (2019).

12. A. Badkar, A. Wolf, L. Bohack, P. Kolhe, Development of biotechnology products in pre-filled syringes: Technical considerations and approaches. *AAPS PharmSciTech* **12**, 564–572 (2011).

13. A. Sreedhara, Z. K. Glover, N. Piros, N. Xiao, A. Patel, B. Kabakoff, Stability of igg1 monoclonal antibodies in intravenous infusion bags under clinical in-use conditions. *J. Pharm. Sci.* **101**, 21–30 (2012).

14. I. C. Shieh, A. R. Patel, Predicting the agitation-induced aggregation of monoclonal antibodies using surface tensiometry. *Mol. Pharm.* **12**, 3184–3193 (2015).

15. D. Graham, M. Phillips, Proteins at liquid interfaces I. Kinetics of adsorption and surface denaturation. *J. Colloid Interface Sci.* **70**, 403–414 (1978).

16. S. J. McClellan, E. I. Franses, Effect of concentration and denaturation on adsorption and surface tension of bovine serum albumin. *Colloids Surf. B Biointerfaces* **28**, 63–75 (2003).

17. J. Penfold, R. K. Thomas, Neutron reflectivity and small angle neutron scattering: An introduction and perspective on recent progress. *Curr. Opin. Colloid Interface Sci.* **19**, 198–206 (2014).

18. C. Stefaniu, G. Brezesinski, X-ray investigation of monolayers formed at the soft air/water interface. *Curr. Opin. Colloid Interface Sci.* **19**, 216–227 (2014).

19. J. Wang, S. M. Buck, Z. Chen, The effect of surface coverage on conformation changes of bovine serum albumin molecules at the air–solution interface detected by sum frequency generation vibrational spectroscopy. *Analyst* **128**, 773–778 (2003).

20. V. S. Alahverdjieva, D. O. Grigoriev, J. K. Ferri, V. B. Fainerman, E. V. Aksenenko, M. E. Leser, M. Michel, R. Miller, Adsorption behaviour of hen egg-white lysozyme at the air/water interface. *Colloids Surf. A Physicochem. Eng. Asp.* **323**, 167–174 (2008).

21. R. Miller, V. B. Fainerman, E. V. Aksenenko, M. Leser, M. Michel, Dynamic surface tension and adsorption kinetics of β-casein at the solution/air interface. *Langmuir* **20**, 771–777 (2004).

22. J. S. Erickson, S. Sundaram, K. J. Stebe, Evidence that the induction time in the surface pressure evolution of lysozyme solutions is caused by a surface phase transition. *Langmuir* **16**, 5072–5078 (2000).

23. S. Sundaram, J. K. Ferri, D. Vollhardt, K. J. Stebe, Surface phase behavior and surface tension evolution for lysozyme adsorption onto clean interfaces and into DPPC monolayers: Theory and experiment. *Langmuir* **14**, 1208–1218 (2002).

24. P. A. Wierenga, M. R. Egmond, A. G. J. Voragen, H. H. J. de Jongh, The adsorption and unfolding kinetics determines the folding state of proteins at the air–water interface and thereby the equation of state. *J. Colloid Interface Sci.* **299**, 850–857 (2006).

25. Y. F. Yano, T. Uruga, H. Tanida, H. Toyokawa, Y. Terada, M. Takagaki, H. Yamada, Driving force behind adsorption-induced protein unfolding: A time-resolved x-ray reflectivity study on lysozyme adsorbed at an air/water interface. *Langmuir* **25**, 32–35 (2009).

26. Y. F. Yano, E. Arakawa, W. Voegeli, C. Kamezawa, T. Matsushita, Initial conformation of adsorbed proteins at an air–water interface. *J. Phys. Chem. B.* **122**, 4662–4666 (2018).

27. C. Postel, O. Abillon, B. Desbat, Structure and denaturation of adsorbed lysozyme at the air–water interface. *J. Colloid Interface Sci.* **266**, 74–81 (2003).

28. V. B. Fainerman, R. Miller, *Proteins at Liquid Interfaces* (Elsevier, 1998).

29. V. Mitropoulos, A. Mütze, P. Fischer, Mechanical properties of protein adsorption layers at the air/water and oil/water interface: A comparison in light of the thermodynamical stability of proteins. *Adv. Colloid Interface Sci.* **206**, 195–206 (2014).

30. F. Höök, M. Rodahl, P. Brzezinski, B. Kasemo, Energy dissipation kinetics for protein and antibody–antigen adsorption under shear oscillation on a quartz crystal microbalance. *Langmuir* **14**, 729–734 (1998).

31. Z. Li, R. Li, C. Smith, F. Pan, M. Campana, J. R. Webster, C. F. van der Walle, S. Uddin, S. M. Bishop, R. Narwal, J. Warwicker, J. R. Lu, Neutron reflection study of surface adsorption of Fc, Fab, and the whole mAb. *ACS Appl. Mater. Interfaces* **9**, 23202–23211 (2017).

32. M. E. Wiseman, C. W. Frank, Antibody adsorption and orientation on hydrophobic surfaces. *Langmuir* **28**, 1765–1774 (2012).

33. N. Chennamsetty, B. Helk, V. Voynov, V. Kayser, B. L. Trout, Aggregation-prone motifs in human immunoglobulin G. *J. Mol. Biol.* **391**, 404–413 (2009).

34. H.-C. Mahler, F. Senner, K. Maeder, R. Mueller, Surface activity of a monoclonal antibody. *J. Pharm. Sci.* **98**, 4525–4533 (2009).

35. T. Serno, E. Härtl, A. Besheer, R. Miller, G. Winter, The role of polysorbate 80 and HPβCD at the air-water interface of IgG solutions. *Pharm. Res.* **30**, 117–130 (2013).

36. E. Koepf, R. Schroeder, G. Brezesinski, W. Friess, The film tells the story: Physical-chemical characteristics of igg at the liquid-air interface. *Eur. J. Pharm. Biopharm.* **119**, 396–407 (2017).

37. A. D. Kanthe, M. Krause, S. Zheng, A. Ilott, J. Li, W. Bu, M. K. Bera, B. Lin, C. Maldarelli, R. S. Tu, Armoring the interface with surfactants to prevent the adsorption of monoclonal antibodies. *ACS Appl. Mater. Interfaces* **12**, 9977–9988 (2020).

38. C. Smith, Z. Li, R. Holman, F. Pan, R. A. Campbell, M. Campana, P. Li, J. R. P. Webster, S. Bishop, R. Narwal, S. Uddin, C. F. van der Walle, J. R. Lu, Antibody adsorption on the surface of water studied by neutron reflection. *MAbs* **9**, 466–475 (2017).

39. Y. S. Tein, Z. Zhang, N. J. Wagner, Competitive surface activity of monoclonal antibodies and nonionic surfactants at the air–water interface determined by interfacial rheology and neutron reflectometry. *Langmuir* **36**, 7814–7823 (2020).

40. A. Tronin, T. Dubrovsky, S. Dubrovskaya, G. Radicchi, C. Nicolini, Role of protein unfolding in monolayer formation on air- water interface. *Langmuir* **12**, 3272–3275 (1996).

41. D. L. Leiske, I. C. Shieh, M. L. Tse, A method to measure protein unfolding at an air-liquid interface. *Langmuir* **32**, 9930–9937 (2016).

42. G. L. Lin, J. A. Pathak, D. H. Kim, M. Carlson, V. Riguero, Y. J. Kim, J. S. Buff, G. G. Fuller, Interfacial dilatational deformation accelerates particle formation in monoclonal antibody solutions. *Soft Matter* **12**, 3293–3302 (2016).

43. A. Kannan, I. C. Shieh, D. L. Leiske, G. G. Fuller, Monoclonal antibody interfaces: Dilatation mechanics and bubble coalescence. *Langmuir* **34**, 630–638 (2018).

44. M. Pershan, P. S. Schlossman, *Liquid Surfaces and Interfaces: Synchrotron X-Ray Methods* (Cambridge Univ. Press, 2012).

45. W. Bu, H. Yu, G. Luo, M. K. Bera, B. Hou, A. W. Schuman, B. Lin, M. Meron, I. Kuzmenko, M. R. Antonio, L. Soderholm, M. L. Schlossman, Observation of a rare earth ion–extractant complex arrested at the oil–water interface during solvent extraction. *J. Phys. Chem. B.* **118**, 10662–10674 (2014).

46. A. Tronin, T. Dubrovsky, C. Nicolini, Comparative study of langmuir monolayers of immunoglobulin G formed at the air-water interface and covalently immobilized on solid supports. *Langmuir* **11**, 385–389 (1995).

47. M. D. Lad, F. Birembaut, J. M. Matthew, R. A. Frazier, R. J. Green, The adsorbed conformation of globular proteins at the air/water interface. *Phys. Chem. Chem. Phys.* **8**, 2179–2186 (2006).

48. S. Damodaran, In situ measurement of conformational changes in proteins at liquid interfaces by circular dichroism spectroscopy. *Anal. Bioanal. Chem.* **376**, 182–188 (2003).

49. G. L. Reddy, R. Nagara, Circular dichroism studies on synthetic signal peptides indicate β-conformation as a common structural feature in highly hydrophobic environment. *J. Biol. Chem.* **264**, 16591–16597 (1989).

50. J. R. Hunter, P. K. Kilpatrick, R. G. Carbonell, Lysozyme adsorption at the air/water interface. *J. Colloid Interface Sci.* **137**, 462–482 (1990).

51. B. Lin, M. Meron, J. Gebhardt, T. Graber, M. L. Schlossman, P. J. Viccaro, The liquid surface/interface spectrometer at ChemMatCARS synchrotron facility at the Advanced Photon Source. *Phys. B Condens. Matter* **336**, 75–80 (2003).

52. M. L. Schlossman, D. Synal, Y. Guan, M. Meron, G. Shea-McCarthy, Z. Huang, A. Acero, S. M. Williams, S. A. Rice, P. J. Viccaro, A synchrotron x-ray liquid surface spectrometer. *Rev. Sci. Instrum.* **68**, 4372–4384 (1997).

53. Molecular Operating Environment (MOE), 2016.0801; Chemical Computing Group Inc: Montreal, QC, Canada (2017).

54. G. T. Tietjen, J. L. Baylon, D. Kerr, Z. Gong, J. M. Henderson, C. T. Heffern, M. Meron, B. Lin, M. L. Schlossman, E. J. Adams, E. Tajkhorshid, K. Y. C. Lee, Coupling x-ray reflectivity and in silico binding to yield dynamics of membrane recognition by tim1. *Biophys. J.* **113**, 1505–1519 (2017).

55. J. K. X. Maier, P. Labute, Assessment of fully automated antibody homology modeling protocols in molecular operating environment. *Proteins* **82**, 1599–1610 (2014).

56. J. R. Biller, H. Elajaili, V. Meyer, G. M. Rosen, S. S. Eaton, G. R. Eaton, Electron spin-lattice relaxation mechanisms of rapidly-tumbling nitroxide radicals. *J. Magn. Reson.* **236**, 47–56 (2013).

57. D. Case, T. Darden, T. E. Cheatham III, C. Simmerling, J. Wang, R. Duke, R. Luo, M. Crowley, R. Walker, W. Zhang, K. Merz, B. Wang, S. Hayik, A. Roitberg, G. Seabra, I. Kolossváry, K. Wong, F. Paesani, J. Vanicek, X. Wu, S. Brozell, T. Steinbrecher, H. Gohlke, L. Yang, C. Tan, J. Mongan, V. Hornak, G. Cui, D. Mathews, M. Seetin, C. Sagui, V. Babin, P. A. Kollman, *Amber 10* (University of California, 2008).